Turbulence Modelling for Supercritical Flows Including Examples with Passive Shock Control

A. Sedaghat, J.A.D. Ackroyd, and N.J. Wood

The Manchester School of Engineering
Aerospace Engineering Division, University of Manchester
Manchester M13 9PL
UK

ABSTRACT

The aerodynamic performance of supercritical aerofoils at transonic speeds is strongly influenced by the shock wave-boundary layer interaction. Passive shock control is one of the techniques used for controlling the undesirable effects of strong shock wave-boundary layer interaction leading to extensive separation. Using passive shock control, the stall margin is increased and the onset of buffeting is delayed. Passive shock control is modelled by introducing a closed plenum chamber underneath a perforated surface at the foot of the shock wave where a combination of blowing and suction is generated. As a result, a strong normal shock wave is changed into a series of weak shock waves with lambda shape. Since the Baldwin-Lomax turbulence model has been used extensively for passive shock control modelling, which exhibits poor predictability for separated flows, an attempt has been made to modify the Reynolds normal stresses for this model so as to improve the accuracy of numerical results for flows with separation. Further modification to the Baldwin-Lomax model has been employed so that the mass transpiration effects are taken into account for the passive shock control computations. In this paper, a brief description on an implicit finite-volume TVD scheme in general coordinates is given and the details of the Balwin-Lomax turbulence model and its modifications are presented. The validated numerical results for several RAE 2822 aerofoil problems plus corresponding results for the modelled methods are presented and compared with some experimental data and other numerical results.

NOMENCLATURE

a^l	eigenvalues of the Jacobian matrices
A^+	Prandtl-Van Driest constant
$\hat{\mathbf{A}}$	Jacobian matrix for the flux vector $\hat{\mathbf{F}}$
$\hat{\mathbf{B}}$	Jacobian matrix for the flux vector $\hat{\mathbf{G}}$
c	aerofoil chord length
c_p	specific heat at constant pressure
C_∞	freestream sound speed
C_p	pressure coefficient
C_D	drag coefficient
C_{wake}	wake constant
C_{kleb}	Klebanoff constant
C_{cp}, C_{cs}	constants in outer eddy viscosity formulation
D	van-Driest damping function
e	total energy per unit volume
$\mathbf{E}^n$	vector of conservative variables at time n
$\mathbf{E}^*$	vector of conservative variables at $n+1/2$
$\mathbf{F}$	flux vector in x direction
$\hat{\mathbf{F}}$	flux vector in ξ direction
F, F_{max}, F_{peak}	blending function F, its max. and peak value
F_{wake}	wake factor
F_{kleb}	Klebanoff intermittency factor
$\mathbf{G}$	flux vector in y direction
$\hat{\mathbf{G}}$	flux vector in η direction
$\mathbf{H}^\xi, \mathbf{H}^\eta$	operator in ξ and η directions
g^l	upwind limiter function
I	4×4 identity matrix
J	Jacobian of transformation
K	von-Karman constant
l_m	Prandtl mixing length
M_∞	freestream Mach number
M_ξ, M_η	scalars of eigenvalues in ξ and η directions
p	pressure
p_∞	freestream pressure
p_w	wall pressure
$\bar{p}$	plenum chamber pressure
p^+	pressure gradient function
Pr_l, Pr_t	laminar and turbulent Prandtl numbers
q_x, q_y	heat flux components
$\mathbf{R}, \mathbf{R}^{-1}$	right eigenvector and its inverse
RHS	Right Hand Side
Re	Reynolds number
t	time
TVD	Total Variation Diminishing scheme
T, T_∞	temperature, freestream temperature
$\mathbf{U}$	vector of conservative variables
U_∞	freestream velocity
U_{diff}	velocity difference

u_τ	friction velocity
u, v	velocity components
$u^{'}, v^{'}$	fluctuating velocity components
v_n	transpiration velocity
v_n^+	scaled transpiration velocity
x, y	Cartesian coordinates

Greek Symbols

α	aerofoil incidence angle
α_{ij}	characteristic speed
ϵ, δ	small constants
Δ	forward difference operator
γ	ratio of specific heats
γ_{ij}	function in the upwind scheme
κ	thermal conductivity coefficient
μ_l	laminar viscosity coef.
μ_t	turbulent viscosity coef.
μ_{ti}, μ_{to}	inner and outer eddy viscosity coef.
Ω^ξ, Ω^η	operator functions
ω	vorticity
$\mathbf{\Phi}$	dissipation function
$(\phi)^U$	upwind dissipation function
ψ	entropy correction function
ρ	density
$\tau_{xx}, \tau_{xy}, \tau_{yy}$	stress tensor components
τ_w	wall shear stress
ξ, η	general coordinate directions
$\xi_x, \xi_y, \eta_x, \eta_y$	partial derivatives
η^+	scaled distance from wall
ν	kinematic viscosity coefficient

1 INTRODUCTION

In order to reduce undesired effects of shock-boundary layer interaction for supercritical aerofoils many different techniques have been used. One of them is the passive control of the interaction region using a porous surface above a closed plenum chamber at the foot of the shock wave. Comprehensive reviews of theoretical and experimental investigations of passive control have been given by Raghunathan[1] and more recently by the European Union[2]. In Raghunathan's review, he concluded that for practical aerofoils the passive control can remove shock buffeting and also can reduce drag at off-design conditions. Recently, more extensive experimental and numerical investigation have been made by the European Union on the subject of drag reduction by passive control. This is now the major reference on the subject of passive drag-reduction which has also cleared up much earlier misunderstanding. In this reference, more practical aerofoil flows without or with small separation have been considered.

A comprehensive study of several advanced turbulence models for solving separated flows over high angle of attack aerofoils has been made by Lien[3]. Lien has concluded that none of the models utilised can predict the onset of separation at the correct angle of incidence and the separation phenomena needed to be further investigated.

In the present study, since the passive control of shock wave-boundary layer interaction with extensive separation is sought, a fairly simple approach is introduced to improve predictability of the Baldwin-Lomax turbulence model for engineering application. This is achieved by modelling the Reynolds normal stresses within the Baldwin-Lomax model. It is observed that with injecting some amount of anisotropy into the turbulence model, the shock wave position and the onset of separation can be better predicted. Darcy's law has been employed as a crude estimation for the modelling of the mass transpiration into the perforated surface so that a comparison of results with Gillan[4] becomes possible. However, the recent European cooperative study has indicated that the Poll[2] model has been more successful than others for predicting the mass transpiration onto the porous surface. In spite of numerous restrictions such as grid resolution, time stepping, domain initialisation, and controlling transpiration velocity that Gillan[4] has employed for his passive control computation, the current study achieves as good results as his with no specific restriction.

An implicit TVD scheme has been selected for this study. The TVD concept was first proposed by Harten[5,6] and then modified and generalised by Yee[7,8,9] who had implemented this so as to solve the two-dimensional Euler equations of gas-dynamics for aerofoil problems. In most of these papers inviscid aerofoil flows have been considered and the interest in general was flow features such as shock capturing. However, in our study we aim to make the scheme a practical tool for computation of transonic flows over aerofoils and examine the ability of the scheme to predict accurately aerodynamic coefficients. The aerodynamic coefficients which are important from a practical point of view cannot be resolved efficiently by the original Yee scheme because of many involved control parameters such as type of limiters, local time-stepping, and dissipation correction at boundaries. Therefore, some modification of the original scheme is introduced[10] to obtain more accurate results.

In the present study, the finite-difference explicit part of the flux computation in Yee's implicit scheme has been replaced by a finite-volume scheme and the implicit part and TVD dissipation functions are also modified. Since at steady-state the solution of implicit schemes converge to the explicit part by vanishing the implicit part, we can claim that the final results are truly based on a finite-volume scheme which is most de-

sirable for aerofoil flows. The derivation of this class of TVD schemes in two-dimensional generalised curvilinear coordinates, and details of this scheme, can be found in references[10,11,12] for compressible flows. Details of the Baldwin-Lomax[13] turbulence model in non-dimensional form used here are explained and the numerical implementation of this turbulent model is discussed. Further modification of the turbulence model due to the modelling of separated flows, and also including transpiration effects, are discussed and the corresponding results are presented.

2 GOVERNING EQUATIONS

The nondimensional form of the compressible Navier-Stokes equations in general curvilinear coordinates in two dimensions can be written as

$$\frac{\partial \hat{\mathbf{U}}}{\partial t} + \frac{\partial \hat{\mathbf{F}}}{\partial \xi} + \frac{\partial \hat{\mathbf{G}}}{\partial \eta} = 0 \tag{1}$$

where

$$\begin{aligned} \hat{\mathbf{U}} &= \mathbf{U}/J \\ \hat{\mathbf{F}} &= (\xi_x \mathbf{F} + \xi_y \mathbf{G})/J \quad , \quad \hat{\mathbf{G}} = (\eta_x \mathbf{F} + \eta_y \mathbf{G})/J \\ J &= \xi_x \eta_y - \xi_y \eta_x \end{aligned} \tag{2}$$

$\xi = \xi(x,y), \eta = \eta(x,y)$ are coordinate transformation functions and J is the Jacobian of the transformation. The vectors $\mathbf{U}$, $\mathbf{F}$, and $\mathbf{G}$ are given by

$$\begin{aligned} \mathbf{U} &= \begin{bmatrix} \rho \\ \rho u \\ \rho v \\ e \end{bmatrix} \\ \mathbf{F} &= \begin{bmatrix} \rho u \\ p + \rho u^2 - \tau_{xx} \\ \rho u v - \tau_{xy} \\ (e+p)u - u\tau_{xx} - v\tau_{xy} + q_x \end{bmatrix} \\ \mathbf{G} &= \begin{bmatrix} \rho v \\ \rho u v - \tau_{xy} \\ p + \rho v^2 - \tau_{yy} \\ (e+p)v - u\tau_{xy} - v\tau_{yy} + q_y \end{bmatrix} \end{aligned} \tag{3}$$

where ρ, u, v, p and e are the density, velocity components along the $x\_$ and $y\_$ directions, static pressure and total energy respectively. The components of the shear-stress tensor and the heat flux vector in non-dimensional form are given by

$$\begin{aligned} \tau_{xx} &= \frac{\mu}{Re}\left(\frac{4}{3}\frac{\partial u}{\partial x} - \frac{2}{3}\frac{\partial v}{\partial y}\right) \\ \tau_{yy} &= \frac{\mu}{Re}\left(\frac{4}{3}\frac{\partial v}{\partial y} - \frac{2}{3}\frac{\partial u}{\partial x}\right) \\ \tau_{xy} &= \frac{\mu}{Re}\left(\frac{\partial u}{\partial y} + \frac{\partial v}{\partial x}\right) \\ q_x &= \frac{-\mu\ \gamma}{(\gamma-1)\ Re\ Pr}\frac{\partial (p/\rho)}{\partial x} \\ q_y &= \frac{-\mu\ \gamma}{(\gamma-1)\ Re\ Pr}\frac{\partial (p/\rho)}{\partial y} \end{aligned} \tag{4}$$

where μ, γ, Pr and Re are the dynamic viscosity, ratio of specific heats, the Prandtl number, and the Reynolds number based on the chord length.

The following non-dimensionalizations are used to write the governing fluid flow equations; all subsequent equations are in this non-dimensional form.

$$x = \frac{x^*}{c} \quad , \quad y = \frac{y^*}{c} \quad , \quad u = \frac{u^*}{U_\infty} \quad , \quad v = \frac{v^*}{U_\infty} \quad , \quad t = \frac{t^*}{c/U_\infty}$$

$$\rho = \frac{\rho^*}{\rho_\infty} \quad , \quad T = \frac{T^*}{T_\infty} \quad , \quad p = \frac{p^*/p_\infty}{\gamma M_\infty^2}$$

$$\mu_l = \frac{\mu_l^*}{\mu_{\infty_l}} \quad , \quad \mu_t = \frac{\mu_t^*}{\mu_{\infty_l}} \quad , \quad \tau_w = \frac{\tau_w^*}{\rho_\infty\ U_\infty^2}$$

where c, ρ_∞, p_∞, and U_∞ are chord length and freestream density, pressure and velocity, respectively. The Mach number is $M_\infty = U_\infty/C_\infty$, C_∞ being the freestream sound speed.

3 NUMERICAL ALGORITHM

The Alternative Direction Implicit (ADI) form of the Linearised Conservative Implicit (LCI) TVD scheme in generalised curvilinear coordinates can be written as[7,10,12]

$$\begin{aligned} \{\mathbf{I} + \Delta t_{ij}\ (\mathbf{H}^\xi_{i+1/2,j} - \mathbf{H}^\xi_{i-1/2,j})\}\frac{\mathbf{E}^*}{J} &= \frac{\mathbf{RHS}}{J} \\ \{\mathbf{I} + \Delta t_{ij}\ (\mathbf{H}^\eta_{i,j+1/2} - \mathbf{H}^\eta_{i,j-1/2})\}\frac{\mathbf{E}^n}{J} &= \frac{\mathbf{E}^*}{J} \end{aligned} \tag{5}$$

where $\mathbf{I}$ is a 4×4 identity matrix, Δt_{ij} is a local time step, J is a local mesh Jacobian and $\mathbf{E}^n = \mathbf{U}^{n+1} - \mathbf{U}^n$ is a vector of conservative variables. The superscripts $n+1$, n, and $*$ denote the time levels $n+1$, n, and $n+1/2$ respectively. The term $\mathbf{RHS}$ representing the explicit part of the numerical scheme is given in Equation (9) and the operators $\mathbf{H}^\xi$ and $\mathbf{H}^\eta$ are defined here as follows

$$\begin{aligned} \mathbf{H}^\xi_{i\pm1/2,j}\mathbf{E}^* &= \frac{1}{2}[\hat{\mathbf{A}}_{i\pm1,j}\mathbf{E}^*_{i\pm1,j} - \mathbf{\Omega}^\xi_{i\pm1/2,j}\mathbf{E}^*] \\ \mathbf{H}^\eta_{i,j\pm1/2}\mathbf{E}^n &= \frac{1}{2}[\hat{\mathbf{B}}_{i,j\pm1}\mathbf{E}^n_{i,j\pm1} - \mathbf{\Omega}^\eta_{i,j\pm1/2}\mathbf{E}^n] \end{aligned} \tag{6}$$

where the Jacobian matrices $\hat{\mathbf{A}}$ and $\hat{\mathbf{B}}$ result from the linearization of the flux vectors $\hat{\mathbf{F}}$ and $\hat{\mathbf{G}}$ respectively[7,10,12]. For steady-state applications

$$\begin{aligned} \mathbf{\Omega}^\xi_{i\pm1/2,j}\mathbf{E}^* &= \pm M^\xi_{i\pm1/2,j}\mathbf{I}(\mathbf{E}^*_{i\pm1,j} - \mathbf{E}^*_{i,j}) \\ \mathbf{\Omega}^\eta_{i,j\pm1/2}\mathbf{E}^n &= \pm M^\eta_{i,j\pm1/2}\mathbf{I}(\mathbf{E}^n_{i,j\pm1} - \mathbf{E}^n_{i,j}) \end{aligned} \tag{7}$$

where the scalar values $M^\xi_{i\pm1/2,j}$ and $M^\eta_{i,j\pm1/2}$ are determined by

$$\begin{aligned} M^\xi_{i\pm1/2,j} &= \max[\psi(a^l_{i\pm1/2,j})] \\ M^\eta_{i,j\pm1/2} &= \max[\psi(a^l_{i,j\pm1/2})] \end{aligned} \tag{8}$$

where $a^l_{i\pm1/2}$ and $a^l_{j\pm1/2}$ are the eigenvalues corresponding to the Jacobian matrices $\hat{\mathbf{A}}$ and $\hat{\mathbf{B}}$ respectively, and ψ is an entropy correction function which is given in Equation (12). The **RHS** in Equation (5) is a combination of a finite-volume[14] approach and the numerical dissipation of the Yee TVD scheme as follows

$$\mathbf{RHS} = -\frac{\Delta t_{i,j}}{A_{i,j}} \sum_{AB}^{DA} (\mathbf{F}\Delta y - \mathbf{G}\Delta x) \qquad (9)$$

$$-\frac{\Delta t_{i,j}}{2}\left[\mathbf{R}_{i+1/2,j}\mathbf{\Phi}_{i+1/2,j} - \mathbf{R}_{i-1/2,j}\mathbf{\Phi}_{i-1/2,j}\right]$$

$$-\frac{\Delta t_{i,j}}{2}\left[\mathbf{R}_{i,j+1/2}\mathbf{\Phi}_{i,j+1/2} - \mathbf{R}_{i,j-1/2}\mathbf{\Phi}_{i,j-1/2}\right]$$

where $\mathbf{F}$ and $\mathbf{G}$ are the flux vectors given in Equation (3), A_{ij} is a local cell area, and $\mathbf{R}_{i\pm1/2,j}$ and $\mathbf{R}_{i,j\pm1/2}$ are the right eigenvectors[7,10,12] of the Jacobian matrices $\hat{\mathbf{A}}$ and $\hat{\mathbf{B}}$ respectively. The function $\mathbf{\Phi}_{i+1/2}$ represented by $(\phi^l_{i+1/2})^U$ for the second-order upwind TVD scheme[10,11] are given as

$$\begin{aligned}(\phi^l_{i+1/2})^U &= \frac{1}{2}\psi(a^l_{i+1/2})(g^l_{i+1} + g^l_i) \\ &- \psi(a^l_{i+1/2} + \gamma^l_{i+1/2})\alpha^l_{i+1/2} \end{aligned} \qquad (10)$$

where α^l is a characteristic function defined in (13), g^l_i is a limiter function given in (14), and the functions γ^l_i and ψ are defined as

$$\gamma^l_{i+1/2} = \frac{1}{2}\psi(a^l_{i+1/2}) \begin{cases} (g^l_{i+1} - g^l_i)/\alpha^l_{i+1/2} & \alpha^l_{i+1/2} \neq 0 \\ 0 & \alpha^l_{i+1/2} = 0 \end{cases} \qquad (11)$$

$$\psi(z) = \begin{cases} |z| & |z| \geq \epsilon \\ (z^2 + \epsilon^2)/2\epsilon & |z| < \epsilon \end{cases} \qquad (12)$$

where ϵ is a small parameter, e.g. $\epsilon = 0.125$. The characteristic function $\alpha^l_{i+1/2}$ is defined as

$$\alpha^l_{i+1/2} = \mathbf{R}^{-1}_{i+1/2}(\mathbf{U}_{i+1} - \mathbf{U}_i) \qquad (13)$$

where $\mathbf{R}^{-1}$ is the inverse of the right eigenvector matrix $\mathbf{R}$. In all test cases, the Van-Leer[10,11] limiter function $g^l_{i+1/2}$ is used

$$\begin{aligned} g^l_i &= \{\alpha^l_{i-1/2}[(\alpha^l_{i+1/2})^2 + \delta] + \alpha^l_{i+1/2}[(\alpha^l_{i-1/2})^2 + \delta]\} \\ &\quad /[(\alpha^l_{i+1/2})^2 + (\alpha^l_{i-1/2})^2 + 2\delta] \end{aligned} \qquad (14)$$

where δ is a small parameter ($10^{-7} \leq \delta \leq 10^{-5}$). In all the above equations Roe's averaging[15] is used to evaluate $\mathbf{U}_{i\pm1/2,j}$, $\mathbf{U}_{i,j\pm1/2}$ and corresponding terms.

4 TURBULENCE MODELLING

For laminar flow computation the coefficient of molecular viscosity μ_l is obtained from Sutherland's law expressed by

$$\mu_l = T^{3/2}\left(\frac{1.0 + C/T_\infty}{T + C/T_\infty}\right) \qquad (15)$$

with $C = 110.4K$ and the coefficient of thermal conductivity κ is specified by

$$\frac{\kappa_l}{c_p} = \frac{\mu_l}{Pr_l}$$

where the laminar Prandtl number Pr_l is a constant equal to 0.72 for air.

For turbulent flow computations, using a zero-equation model, the transport coefficients in the Navier-Stokes equations are simply replaced by

$$\begin{aligned} \mu &= \mu_l + \mu_t \\ \frac{\kappa}{c_p} &= \frac{\mu_l}{Pr_l} + \frac{\mu_t}{Pr_t} \end{aligned} \qquad (16)$$

where the turbulent Prandtl number is a constant equal to 0.9 for air and the turbulent viscosity coefficient μ_t is computed here using the isotropic, two-layer, Cebeci-type, algebraic eddy-viscosity model reported by Baldwin and Lomax[13].

In the Baldwin-Lomax two-layer formulation μ_t is given by:

$$\mu_t = \begin{cases} \mu_{ti} & , \quad \eta \leq \eta_c \\ \mu_{to} & , \quad \eta > \eta_c \end{cases} \qquad (17)$$

where η is the local distance measured normal to the body surface and η_c is the smallest value of η at which the inner (μ_{ti}) and outer (μ_{to}) eddy viscosity coefficients are equal. In practice, η_c is determined to be the η at which $\mu_{ti} \geq \mu_{to}$ and a hyperbolic tangent function is used which produces a smoother, more desirable eddy viscosity distribution than Equation (17):

$$\mu_t = \mu_{to} \tanh\left(\frac{\mu_{ti}}{\mu_{to}}\right) \qquad (18)$$

Within the inner region, the eddy viscosity coefficient is given by

$$\mu_{ti} = Re_\infty \ \rho \ l^2_m(\eta) \ \ |\omega| \qquad (19)$$

where ρ is the density, Re_∞ is the freestream Reynolds number, $l_m(\eta)$ is the Prandtl mixing length which is given below in (21) and ω is the vorticity defined by

$$\omega = \frac{\partial u}{\partial y} - \frac{\partial v}{\partial x} \qquad (20)$$

where u and v are the Cartesian components of the velocity vector. The Prandtl mixing length l_m is a length scale which is taken to be proportional to the distance η from the wall:

$$l_m(\eta) = K\eta D \qquad (21)$$

Here $K = 0.41$ is the von-Karman constant and D, the Van-Driest damping function, is given by

$$D = [1 - \exp(-\eta^+/A^+] \qquad (22)$$

where $A^+ = 26$ is the surface factor for a smooth wall. The function η^+ is defined as

$$\eta^+ = \frac{Re_\infty \eta}{\mu_{l_w}} \sqrt{\rho_w \tau_w} \tag{23}$$

where μ_{l_w} is the molecular viscosity at the wall and τ_w, the shear stress tangential to the wall, is approximated by

$$\tau_w = \frac{\mu_w}{Re_\infty} \left(\frac{\partial U_t}{\partial \eta} \right)_w \tag{24}$$

where U_t is the mean-velocity component tangential to the surface. In the outer region ($\eta \geq \eta_c$) the eddy viscosity is given by

$$\mu_{to} = Re_\infty \ \rho \ C_{cs} \ C_{cp} \ F_{wake} / F_{kleb} \tag{25}$$

where $C_{cs} = 0.0168$ and $C_{cp} = 1.6$ are constants, F_{kleb} is the Klebanoff intermittency factor given in (28) and F_{wake} is determined from

$$F_{wake} = \min \left\{ \eta_{max} F_{max}, \frac{C_{wake} \eta_{max} U_{dif}^2}{F_{max}} \right\} \tag{26}$$

where $C_{wake} = 0.25$ is a constant, $U_{dif} = U_{max} - U_{min}$ is the maximum velocity difference across the boundary layer, η_{max} is the distance from the wall at which $F(\eta)$ becomes maximum. F_{max} is the maximum value of the function $F(\eta)$ given as

$$F(\eta) = \frac{l_m(\eta)}{K} \mid \omega \mid \tag{27}$$

where the vorticity, ω, and the Prandtl mixing length, $l_m(\eta)$, are given in equations (20) and (21) respectively. F_{kleb} is the Klebanoff intermittency factor defined as

$$F_{kleb} = \left[1.0 + 5.5 \left(\frac{C_{kleb} \ \eta}{\eta_{max}} \right)^6 \right] \tag{28}$$

where $C_{kleb} = 0.3$ is the Klebanoff constant.

The maximum value of the function F in Equation (27), F_{max}, is found by a search across the boundary layer at each station and η_{max} refers to the position where F_{max} occurs. The length scale η_{max} is used as a characteristic scale for the outer part of the boundary layer, so that near wall peaks in F must be ignored. This is accomplished by restricting the search for F_{max} to $\eta^+ > 10$. Secondly, multiple peaks in F may occur, particularly downstream of shock waves. An effective strategy used by Johnston[16] is to search across the boundary layer, starting at $\eta^+ > 10$, for the first three peaks and to take the largest of these peaks to determine η_{max}. To determine each peak in F, the method suggested by Degani[17] is modified and defined by

$$\begin{aligned} if \quad & (F_{i,j} > F_{i,j+1} \quad and \quad F_{i,j} > F_{i,j-1}) \\ & then \quad F_{peak} = F_{i,j} \end{aligned} \tag{29}$$

where $F_{i,j-1}, F_{i,j}$ and $F_{i,j+1}$ correspond to the normal distances from the wall, $\eta_{i,j-1}, \eta_{i,j}$ and $\eta_{i,j+1}$, respectively. In the wake region a simple wake model is used, i.e. the upper and lower surface trailing edge eddy-viscosity distributions are imposed at all stations downstream in the wake:

$$\begin{cases} (\mu_t)^U_{wake} = (\mu_t)^U_{t.e.} \\ (\mu_t)^L_{wake} = (\mu_t)^L_{t.e.} \end{cases} \tag{30}$$

As far as the flow development around the aerofoil is considered, the above approximation for the immediate near-wake region gives a reasonable estimation.

4.1 Turbulence Model Modification for Separated Flows

In the literature, many numerical results based on various turbulence models can be found which show poor predictability for separated flows, especially when a strong shock wave boundary layer interaction has occurred[18,19,20] over the upper aerofoil surface. In most transonic aerofoil computations, mismatch of the shock wave position has been reported for these types of flows where the effects of using different turbulence models have been investigated. In this section, a preliminary modification to the Baldwin-Lomax turbulence model is introduced for the better prediction of separated flows in the presence of a strong shock wave. The aim is to provide a practical tool from the modified model for the computation of passively controlled problems with strong separation.

When an algebraic turbulence model such as Baldwin-Lomax is considered, the Reynolds stresses are modelled in a manner similar to the laminar stresses in the Navier-Stokes equations. Thus, the approximated Reynolds stresses are given as follows:

$$\begin{aligned} -\overline{\rho u'^2} &= \frac{\mu_t}{Re} \left(\frac{4}{3} \frac{\partial u}{\partial x} - \frac{2}{3} \frac{\partial v}{\partial y} \right) \\ -\overline{\rho u' v'} &= \frac{\mu_t}{Re} \left(\frac{\partial u}{\partial y} + \frac{\partial v}{\partial x} \right) \\ -\overline{\rho v'^2} &= \frac{\mu_t}{Re} \left(\frac{4}{3} \frac{\partial v}{\partial y} - \frac{2}{3} \frac{\partial u}{\partial x} \right) \end{aligned} \tag{31}$$

where μ_t is the the eddy viscosity coefficient. There are two important shortcomings for such a model. First, the terms $\overline{\rho u'^2}$ and $\overline{\rho v'^2}$ are positive whereas the above expressions do not ensure this positiveness. Second, from the Baldwin-Lomax numerical results it has been observed that the Reynolds normal stresses, without including $\frac{2}{3}\rho k$, are too small compared with the experimental results, a conclusion which contrasts with the relatively good agreement between the numerical and the experimental values of the Reynolds shear stress.

A comprehensive experimental study over a bump flow

reported by Delery[21] has indicated that the Reynolds normal stresses can be as big as, or sometimes several times bigger than, the Reynolds shear stress. Delery's test case C has been the toughest of his series which has been computationally investigated in several CFD workshops, of which the UMIST ERCOFTAC STG workshop[20] is the latest one. In spite of requesting the presentation of all the Reynolds stresses at several locations, most of the contributors have merely presented the Reynolds shear stress values which are relatively close to the measurements. Our computation for this test case, using the Baldwin-Lomax model, indicates that the resulting Reynolds normal stresses are too small or in fact negligible. The Baldwin-Lomax model may be a very good choice with which to examine the effects of the modelled Reynolds normal stresses which are going to be introduced.

Considering these facts, and also the work by Lien[2] for 2D separated flows around an aerofoil section, it is concluded that the Reynolds normal stresses can be related to the Reynolds shear stress by introducing local equilibrium constraints (see Lien[2]). In general, the following expressions can be derived

$$\begin{aligned} \overline{\rho u'^2} &= C_1 |\overline{\rho u' v'}| \\ \overline{\rho v'^2} &= C_2 |\overline{\rho u' v'}| \end{aligned} \tag{32}$$

Lien has derived relations for the Reynolds stresses using several turbulence models from the non-linear $(k-\epsilon)$ eddy viscosity models to the Reynolds Stress Turbulence Models (RSTM) assuming the local equilibrium condition. Based on his complete model for the RSTM, the values of $C_1 = 4.3185$ and $C_2 = 0.9234$ can be obtained so as to inject a reasonable degree of anisotropy into the Baldwin-Lomax model.

4.2 Turbulence Model Modification for Porous Surfaces

The transpiration velocity on a porous surface has been modelled via Darcy's law[22] in some earlier computational investigations[4,23]. Darcy's law states that the transpiration velocity through a porous medium is linearly proportional to the pressure drop across that medium. In non-dimensional form Darcy's law may be written as

$$v_n = -\bar{\sigma} \Delta p \tag{33}$$

where

$$\Delta p = (p_w - \bar{p}) \tag{34}$$

with v_n, p_w, $\bar{p}$, and $\bar{\sigma}$ represent the normal wall velocity at the porous surface, the wall pressure, the plenum pressure and the porosity distribution function, respectively. The porosity distribution function, $\bar{\sigma}$, depends on both the fluid viscosity and the size and spacing of the holes in the porous surface. A physical restriction observed from experimental investigations is that the porous induced velocity should not exceed the limit of 5% of the freestream velocity. Since the plenum is a closed chamber except for the porous surface, the net mass flow rate over this porous surface is zero, i.e.,

$$\int_S \rho_w v_n \, dS = 0 \tag{35}$$

Thus using equations (33) and (34), the plenum pressure can be determined as follows:

$$\bar{p} = \frac{\int_S \rho_w p_w \, dS}{\int_S \rho_w \, dS} \tag{36}$$

The transpiration velocity, v_n, may now be calculated using Equation (35) in conjunction with the above definition for $\bar{p}$.

Due to the transpiration through the porous region, the turbulence model must be modified to include the effects of flow laminarisation. To include this mass-transfer effect on the Baldwin-Lomax turbulent model, the Prandtl-Van Driest constant, A^+, is redefined for the inner region as suggested in reference[23]:

$$A^+ = 26 \left\{ -\frac{p^+}{v_n^+} \left[\exp(11.8 \, v_n^+) - 1 \right] + \exp(11.8 v_n^+) \right\}^{-\frac{1}{2}} \tag{37}$$

where

$$v_n^+ = \frac{v_n}{u_\tau} \tag{38}$$

$$p^+ = \frac{-Re_\infty^{-1} \nu_{wl}}{\rho_w u_\tau^3} \left(\frac{dp}{d\xi} \right)_w \tag{39}$$

and ξ is the direction tangent to the surface, $(dp/d\xi)_w$ is the pressure gradient at the wall in the ξ direction, ν_{wl} is the laminar kinematic viscosity at the wall and u_τ is the friction velocity given by

$$u_\tau = \sqrt{|\tau_w| / \rho_w} \tag{40}$$

where ρ_w and τ_w are the density and the tangential shear stress at the wall, respectively.

The change in A^+ was first proposed by Cebeci[24] and then modified by Chokani & Squire[23] to account for the changes in the law-of-the-wall and in skin friction caused by suction and blowing. The modification yields the result that the skin friction is reduced in the blowing region ($v_n^+ > 0$) and in adverse pressure gradients with the converse effect in regions of suction and of favourable pressure gradient.

For a porous flat-plate flow, Equation (37) reduces to

$$A^+ = 26 \, \exp(-5.9 \, v_n^+) \tag{41}$$

This has been used by some authors as a simple approximation for aerofoil passive control[4,23]. In this research,

no noticeable improvement was observed using Equation (37); therefore, Equation (41) has been used for the current computations. Further modification has been made to the Baldwin-Lomax model to improve convergence of the numerical scheme in the presence of porous transpiration. The wall shear stress, τ_{wall} in Equation (23), was replaced by the maximum boundary layer shear stress, τ_{max}, obtained in a plane parallel to the aerofoil surface.

5 RESULTS AND DISCUSSION

Results are presented in this section of calculations for the RAE 2822 covering a range of conditions from fully subcritical flow to supercritical flow with shock-induced separation. The calculations are made using the method with a fixed set of flow algorithm and grid generation parameters.

Computational grids are constructed using the algebraic grid generator of Rizzi[25] together with a hyperbolic grid generator of Alsalihi[26] to produce an orthogonal C-mesh for the test cases; see Fig. 3.b. A relatively coarse mesh of 141×61 has been used in order to investigate performance of the numerical results. The outer boundary is placed at 18 chord lengths away from the aerofoil surface. The first cell-size at both the leading edge and the trailing edge is fixed as $\frac{\Delta\xi}{c} = 0.002$ and $\frac{\Delta\eta}{c} = 0.00002$. In the wake region 24×61 grid points have been placed between the upper and the lower wake cut and the outflow boundary which is placed 10 chord lengths downstream of the trailing edge.

Each test case was initialised with a uniform freestream flow at the prescribed Mach number and angle of attack. The no-slip condition together with zero normal pressure gradient and normal temperature gradient (adiabatic wall) have been applied at the aerofoil surface. The characteristic boundary condition[27] has been used for the outer boundary and zero extrapolation was used for the outflow boundary. In the wake region simple averaging has been applied to all conservative variables.

A local time-stepping similar to Pulliam and Steger[7] is used here and is based on mesh Jacobians as follows:

$$\Delta t_{i,j} = \frac{S}{1 + \sqrt{J_{i,j}}} \qquad (42)$$

S being a constant to provide the maximum allowed time-step which can maintain the stability of the numerical scheme. A typical value used in our computation for S is 0.5.

The RAE 2822 aerofoil has been designed for transonic flows and has a maximum thickness/chord ratio of 12.1 % and a sharp trailing edge. An extensive experimental study of this aerofoil in the 8ft $\times$ 6ft transonic wind tunnel at RAE Farnborough was presented by Cook *et al*[28]. This case has been used extensively to validate numerical methods[18].

TABLE 1
RAE 2822 Aerofoil
Results using Baldwin-Lomax (B-L) model
(a) Flow conditions

Case	M	α	$R_e \times 10^{-6}$
1	0.676	1.93^o	5.7
6	0.725	2.54^o	6.5
9	0.730	2.79^o	6.5
10	0.750	2.81^o	6.2

b) Comparison of measured and calculated loads

Case 1	C_L	C_D	$C_M(1/4)$
Experiment	0.566	0.0085	-0.082
Johnston (B-L)	0.5802	0.01068	-0.08769
present (B-L)	0.5677	0.009544	-0.08488

Case 6	C_L	C_D	$C_M(1/4)$
Experiment	0.743	0.0127	-0.095
Johnston (B-L)	0.7457	0.01502	-0.09175
present (B-L)	0.7457	0.01311	-0.09001

Case 9	C_L	C_D	$C_M(1/4)$
Experiment	0.803	0.0168	-0.099
Johnston (B-L)	0.7950	0.01884	-0.09513
present (B-L)	0.8034	0.01638	-0.09298

Case 10	C_L	C_D	$C_M(1/4)$
Experiment	0.743	0.0242	-0.106
Johnston (B-L)	0.7901	0.02921	-0.1108
present (B-L)	0.7982	0.02514	-0.1074
modified (B-L)	0.6913	0.0201	-0.0823

A close-up of the computational grid around the RAE 2822 aerofoil is shown in Fig. 3.b. Four cases are considered here and the relevant flow conditions are given in Table 1(a). Comparisons of predicted and measured lift, drag and pitching moment coefficients together with Johnston's[16] numerical results are shown in Table 1(b), the results being presented for the Baldwin-Lomax turbulence model. Note that Johnston's results are based on a fairly fine mesh consisting of 272×64 cells.

Transition is fixed at 11 % chord for Case 1 and at 3 % chord for the others on the upper and lower surfaces of the aerofoil. A brief discussion on the results obtained for the Cases 1, 6, and 9 are given below; the interested reader is reffered to Sedaghat[10] for more details and the corresponding graphs. Case 10 is studied here in more details.

Considering the Case 1 which involves mainly subcritical flow, the agreement with measurements is fairly good, drag prediction being very close to experiment.

Case 6 presents a supercritical flow on the upper surface terminated by a shock wave of moderate strength just downstream of the mid-chord position. Drag and moment coefficients predicted by the present method are in good agreement with measurements.

Most aerodynamic coefficients are matched closely with the measurements for Case 9. The upper surface skin friction distribution in ref.[10] indicates flow separation at the foot of the shock wave for the Baldwin-Lomax turbulent model. No separation in the experiment is reported for this case[28]. This tendency of the Baldwin-Lomax model to predict premature flow separation, particularly at shock waves, has been noted by other authors[18].

5.1 The Test Case with Separation

From the literature, no modification to the turbulence models utilised in this work has been introduced to improve solutions when a strong shock wave boundary layer interaction occurred over the upper aerofoil surface. Recently, Taki[29] has modified the Reynolds stresses in the one-equation ($k - L_\epsilon$) model and taken them from the latest Reynolds Stress Models (RSM). However, no very close agreement for the pressure distribution has been achieved when compared with experiment.

Case 10 is the most interesting of the RAE2822 cases to be considered, since it is the only one in which shock-induced separation was observed in the experiment. The original Baldwin-Lomax model and its modified version introduced in section 4.1. are considered here and the corresponding results are compared. The drag and moment coefficients have been predicted unexpectedly fairly close to experiment using the original model. However, the lift coefficient has not been accurately predicted using both models (see table 1.b). A stronger shock wave appeared on the upper aerofoil surface, Fig. 1, and a larger supersonic region is formed between the leading edge and the shock wave. Convergence is only achieved after 2000 iterations (Fig. 2) for both models. In Fig. 3.a, it is shown that there are now larger discrepancies between prediction and measurement of the shock wave position for the original model, but the shock wave position has exactly matched experiment using the modified model. From the computation of the upper surface skin friction in Fig. 3.d, it is observed that the flow remains separated up to the trailing edge for the Baldwin-Lomax turbulent model. This behaviour has not been observed experimentally. The turbulence model has failed to predict the correct shock wave position. Bigger discrepancies are observed, Fig. 4, between computation and experiment for the boundary layer displacement thickness than for the momentum thickness distribution. The velocity profiles presented in Figs. 5 and 6 also indicate bigger differences between predicted and measured profiles. However, slightly better results are observed using the modified Baldwin-Lomax model for the surface skin friction coefficients, Figs. 3.c and 3.d., the boundary layer displacement and momentum thicknesses, Fig. 4, and the velocity profiles in Figs. 5 and 6. At least, the current modification of the Baldwin-Lomax model has yield to a better prediction on the shock wave position. Furthermore, this experiment as reported by Cook *et al*[28] was not exactly 2D.

5.2 The Test Cases with Porous Surface

Transonic flow computations were performed around a modified non-lifting porous RAE2822 aerofoil section similar to that employed by Chen *et al*[22]. The modified RAE2822 aerofoil was generated by reflecting the original RAE2822 design upper surface definition onto its lower surface, thereby creating a non-lifting symmetrical section. As in section 5, a 141×61 orthogonal C-grid was employed, with the far-field boundary located at approximately 18 chord lengths. The same initial spacings as in section 5 were employed.

Two particular flow conditions similar to that considered by Gillan[4] have been studied, namely cases 1 and 2, with freestream Mach numbers corresponding to $M_\infty = 0.81$ and $M_\infty = 0.85$ respectively. For both of the cases, computations were conducted at zero incidence with a freestream Reynolds number of $Re_\infty = 6.5 \times 10^6$. Transition to turbulence was fixed at 3% of chord on both the upper and the lower aerofoil surfaces. A similar porous configuration to that used by Gillan[4] was employed. The porous surface region was located from $x = 0.587$ to $x = 0.904$ on both the upper and the lower surfaces. Furthermore, a constant porosity distribution, $\bar{\sigma} = 0.4$, was used. This distribution induced transpiration velocities less than 5% of the freestream flow velocity and these are therefore consistent with Darcy's law.

The calculations have been made using the finite-volume, implicit, upwind TVD scheme with the modified Baldwin-Lomax model for porous surfaces described in section 4.2. Each test case was initialised with a uniform freestream flow at the prescribed Mach number and angle of attack and the same boundary conditions were employed as described in section 5. The only difference was that the transpiration velocity distribution was taken into account in determining conservative variables over the porous surfaces. Similar local time-stepping, Equation (42), was used; 5000 iterations were performed to obtain a converged solution. The RMS of the averaged density residual was reduced to $(10^{-4} - 10^{-5})$ at the steady-state. No special treatments for the grid,

the time stepping, domain initialisation, and controlling transpiration velocity have been required for the current CFD code despite many restrictions that Gillan has employed for all of them.

5.2.1 Case 1: $M = 0.81, \alpha = 0.0^o, R_e = 6.5 \times 10^6$

Computational results for this case are presented in Figs. 7 and 8 for the symmetric RAE2822 aerofoil both with and without porous regions. From the contour plots of pressure and Mach number, Figs. 7.a and 7.b, an almost moderate normal shock wave is observed with an induced separated flow near the trailing edge of the passively controlled aerofoil. The expected lambda shape of the shock wave cannot be observed clearly in the contour plots.

The drag coefficient has converged to its steady-state value by around 3000 iterations, Fig. 7.c. The values of $C_{DP} = 0.02377$ and $C_{DS} = 0.01653$ were obtained for the porous and the solid aerofoils, respectively. The total drag was increased in this case by the introduction of a porous region. A drag rise has also been reported by Gillan[4], $C_{DP} = 0.0243$ and $C_{DS} = 0.0190$, who used a very fine grid of 400×81. The RMS of the averaged density residual, Fig. 7.d, reached around 10^{-5} for both of the solutions.

The current computed surface distributions are very similar to those obtained by Gillan. Referring to Fig. 8.e, passive control has dramatically reduced the substantial pressure gradients with the original relatively strong shock wave replaced by a weaker lambda shock system. The aforementioned trailing-edge separation regions are apparent in the corresponding skin friction plot (Fig. 8.g). Moreover, the figure also indicates a substantial reduction in the skin friction at the start of the porous region with a relatively constant value in the blowing region. A negative spike is detected in the skin friction in the suction region.

Finally, the computed transpiration velocity distribution is presented in Fig. 8.h. A maximum velocity of approximately 5% of freestream is observed at the rear of the porous region which is in agreement with Darcy's law.

5.2.2 Case 2: $M = 0.85, \alpha = 0.0^o, R_e = 6.5 \times 10^6$

Computational results for this case are presented in Figs. 9 and 10 considering both the symmetric RAE2822 aerofoil with and without porous regions. Case 2 represents a significantly more challenging problem for computational methods than the previous case due to the presence of extensive shock-induced separation over the solid aerofoil. From the contour plots of pressure and Mach number, Figs. 9.a and 9.b, a strong normal shock wave is observed with an induced separated flow after it for the porous aerofoil. Again the expected lambda shape of the shock wave cannot be observed clearly in the contour plots.

The drag coefficient converged to its steady-state value around 3000 iterations, Fig. 9.c. The values of $C_{DP} = 0.0505$ and $C_{DS} = 0.0523$ were obtained for the porous and the solid aerofoils, respectively. The total drag was decreased by about 3.4% in this case with the introduction of the porous region. The drag reduction has also reported by Gillan[4] with values $C_{DP} = 0.0510$ and $C_{DS} = 0.0547$. The RMS of the averaged density residual reached around 10^{-4} for porous and 10^{-5} for solid aerofoil solutions. The effect that shock-induced separation has on the residuals may be seen in Fig. 9.d. This non-monotonic nature of the residual has also been reported by Gillan.

In general, the current computed surface distributions are very similar to those obtained by Gillan. As in case 1, the pressure distribution indicates a significant reduction in the large pressure gradients which are presented in Fig. 10.e. Porosity results in the replacement of the original strong shock with a weaker lambda shock system.

The separation regions are clearly shown in the corresponding skin friction plot (Fig. 10.g). As in case 1, the figure also indicates a substantial reduction in the skin friction at the start of the porous region with a relatively constant value in the blowing region. A negative spike is detected in the skin friction in the suction region. Once more, the computed transpiration velocity distribution with a maximum of approximately 5% of freestream is observed in Fig. 10.h, which is in agreement with Darcy's law.

6 CONCLUSION

In this study, a fast algorithm utilising a finite-volume, upwind, implicit, and Total Variation Diminishing (TVD) scheme has been developed and validated against some experimental and other numerical results for turbulent transonic flows over supercritical aerofoils. A hyperbolic C-mesh has been used to provide an orthogonal grid around aerofoil sections. This study has shown that aerodynamic coefficients can be predicted fairly accurately by the TVD algorithm using a relatively coarse orthogonal grid.

In spite of numerous restrictions such as grid resolution, time stepping, domain initialisation, and controlling transpiration velocity as employed by Gillan[4], no specific restrictions are required for the current passive control computation using the inherent advanced TVD property within the numerical algorithm.

Modifying the Reynolds normal stresses for the Baldwin-Lomax turbulence model has improved the prediction of the shock wave position and the onset of separation for the considered test case. Furthermore, the positiveness of the terms $\overline{\rho u'^2}$ and $\overline{\rho v'^2}$, maintained during the numerical procedure for separated flows, should not be overlooked. The current modification to the Baldwin-Lomax turbulence model would certainly require further consideration and development, and this is the subject of further study.

REFERENCES

1. Raghunathan, S. Passive control of shock-boundary layer interaction, *Prog Aerospace Sci*, 1988, **25**, pp 271-296.

2. Stanewsky, E., Delery, J., Fulker, J. and Geiβler, W. EUROSHOCK- Drag reduction by passive shock control, *Notes on Numerical Fluid Mechanics*, **56**, Vieweg, 1997.

3. Lien, F. S. and Leschziner, M. A. Modelling 2D separation from a high lift aerofoil with a non-linear eddy-viscosity model and second-moment closure, *Aeronautical J*, April 1995, (2062), pp 125-144.

4. Gillan, M. A. A Computational Analysis of Viscous Flow Over Porous Aerofoils, *PhD Thesis*, The Queen's University of Belfast, May 1993.

5. Harten, A. A high resolution scheme for the computation of weak solutions of hyperbolic conservation laws, *J Comp Phys*, 1983, **49**, pp 357-393.

6. Harten, A. On a class of high resolution total-variation-stable finite difference schemes, *SIAM J Numer Anal*, 1984, **21**, pp 1-23.

7. Yee, H. C., Warming R. F. and Harten A. Implicit total variation diminishing (TVD) schemes for steady-state calculations, *J Comp Phys*, 1985, **57**, pp 327-360.

8. Yee, H. C. Linearised form of implicit TVD schemes for the multidimensional Euler and Navier-Stokes equations, *Int J on Comp and Math with Appl*, 1986, 12 A, (4/5), pp 413-432.

9. Yee, H. C., Klopfer, G. H. and Montagne, J. L. High-resolution shock-capturing schemes for inviscid and viscous hypersonic flows, NASA TM-100097, April 1990.

10. Sedaghat, A., Shahpar, S. and Hall, I. M. Drag reduction for supercritical aerofoils, *20th ICAS Congress*, Sorrento, Italy, September 1996.

11. Yee, H. C. and Harten A. Implicit TVD schemes for hyperbolic conservation laws in curvilinear coordinates, *AIAA J*, 1986, **25**, (2), pp 226-274.

12. Sedaghat, A., Shahpar, S. and Hall, I. M. A mixed finite-difference & finite-volume TVD scheme for computation of transonic flows, First International Symposium on Finite-Volumes for Complex Applications, Problems, and Perspectives, Rouen, Hermes, Paris, July 1996, pp 317-322.

13. Baldwin, B. and Lomax, H. Thin layer approximation and algebraic model for separated turbulent flows, AIAA Paper 78-257, 1978.

14. Fletcher, C. A. J. Computational Techniques for Fluid Dynamics, Springer-Verlag, 1988.

15. Roe, P. L. Approximate Riemann solvers, parameter vectors, and difference schemes, *J Comp Phys*, 1981, **43**, pp 357-372.

16. Johnston, L. J. Solution of the Reynolds-averaged Navier-Stokes equations for transonic aerofoil flows, *Aeronautical J*, 1991, pp 253-273.

17. Degani, D. and Schiff, L. B. Computation of supersonic viscous flows around pointed bodies at large incidence, AIAA Paper 83-0034, 1983.

18. Holst, T. L. Viscous Transonic Airfoil Workshop compendium of results, AIAA Paper 87-1460, 1987; *J Aircraft*, 1988, **25**, (12), pp 1073-1087.

19. Batten P., Loyau H. and Leschziner, M. A. ERCOFTAC Workshop on Shock/Boundary-Layer Interaction, UMIST, 25-26 March 1997.

20. Leschziner, M. A. EUROVAL: an European Initiative on Validation of CFD Codes, Turbulent Flow Validation Symposium, Braunschweig/Wiesbaden: Vieweg, 1993.

21. Delery, J., Copy, C. and Reisz, J. Analyse au velocimetre laser bidirectionnel dune interaction choc-couche limite avec decollement etendu, *ONERA Report Technique*, 37:7078 AY014, 1980.

22. Chen, C. L., Chow, C. Y., Dalsem, W. R. V. and Holst, T. L. Computation of viscous transonic flow over porous airfoils, *J Aircraft*, December 1989, **26**, (12), pp 1067-1075.

23. Chokani, N. and Squire, L. C. Transonic shock-wave/turbulent boundary layer interactions on a porous surface, *Aeronautical J*, May 1993, pp 163-170.

24. Cebeci, T. Behaviour of turbulent flow near a porous wall with pressure gradient, *AIAA J*, 1970, **82**, pp 2152-2156.

25. Rizzi, A. and Vivand H. Numerical methods for the computation of inviscid transonic flows with shock waves, *Notes on Numerical Fluid Mechanics*, **3**, Vieweg, 1981.

26. Alsalihi, Z. Two dimensional hyperbolic grid generation, *Von Karman Institute for Fluid Dynamics*, Technical Note 162, October 1987.

27. Jameson, A. and Baker, T. J. Solution of the Euler equations for complex configurations, AIAA Paper 83-1929, 1983.

28. Cook, P. H., McDonald, M. A. and Firmin, M. C. P. Aerofoil RAE 2822 - Pressure Distribution, and Boundary Layer and Wake Measurements, AGARD AR 138, A6, May 1979.

29. Taki, M. Computation of the Aerodynamic Performance of High-Lift Aerofoil System at Low Speed and Transonic Flow Conditions, *PhD Thesis*, UMIST, May 1997.

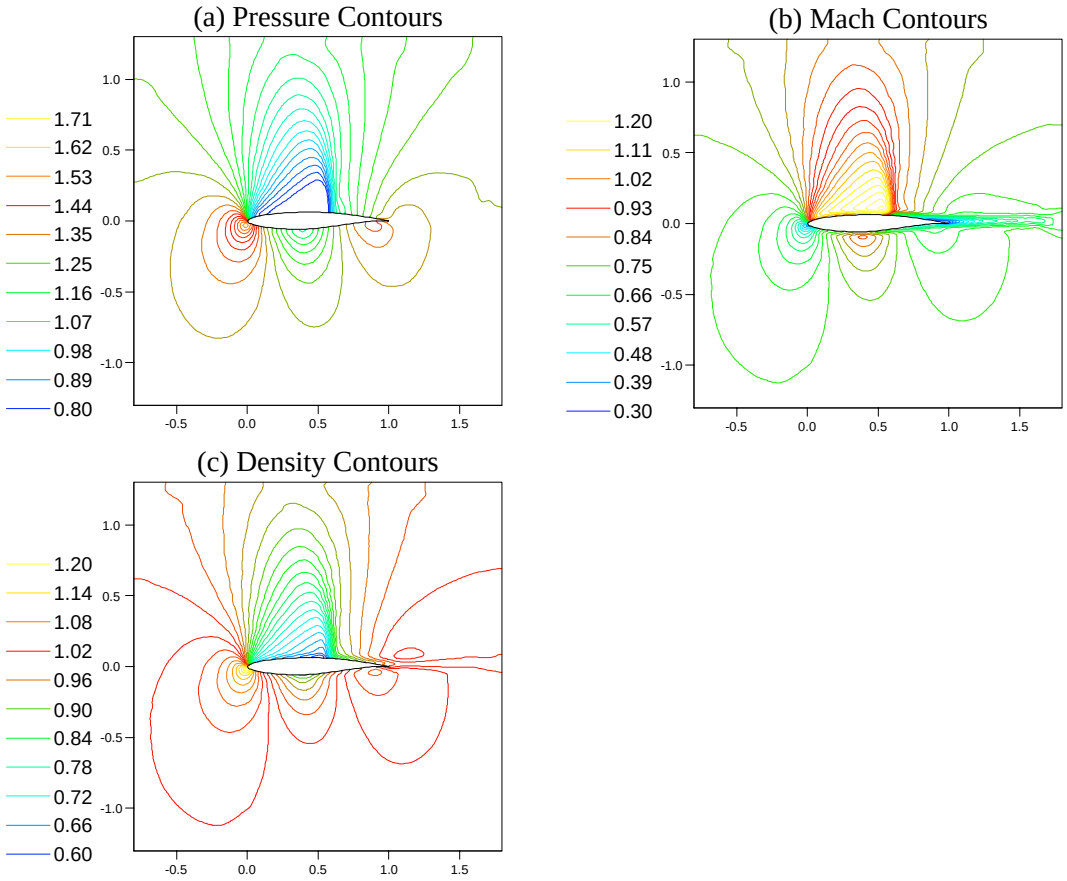

Figure 1: Contour plots of the results obtained for the RAE2822 aerofoil test case (10) using the modified Baldwin-Lomax model; $M = 0.725, \alpha = 2.54^o, R_e = 6.5 \times 10^6$.

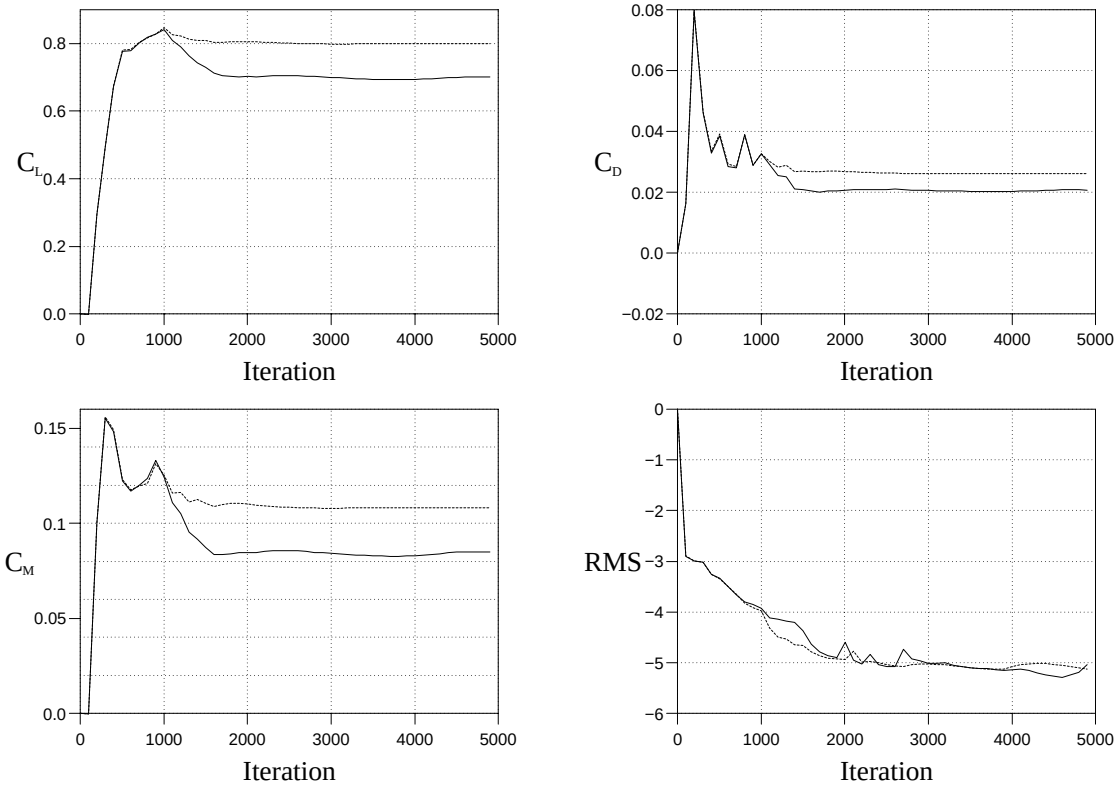

Figure 2: Convergence history of lift coefficient (C_L), drag coefficient (C_D), moment coefficient (C_M), and RMS of density for RAE2822 (case 10) using the modified Baldwin-Lomax (filled line) and Baldwin-Lomax (dashed line) models.

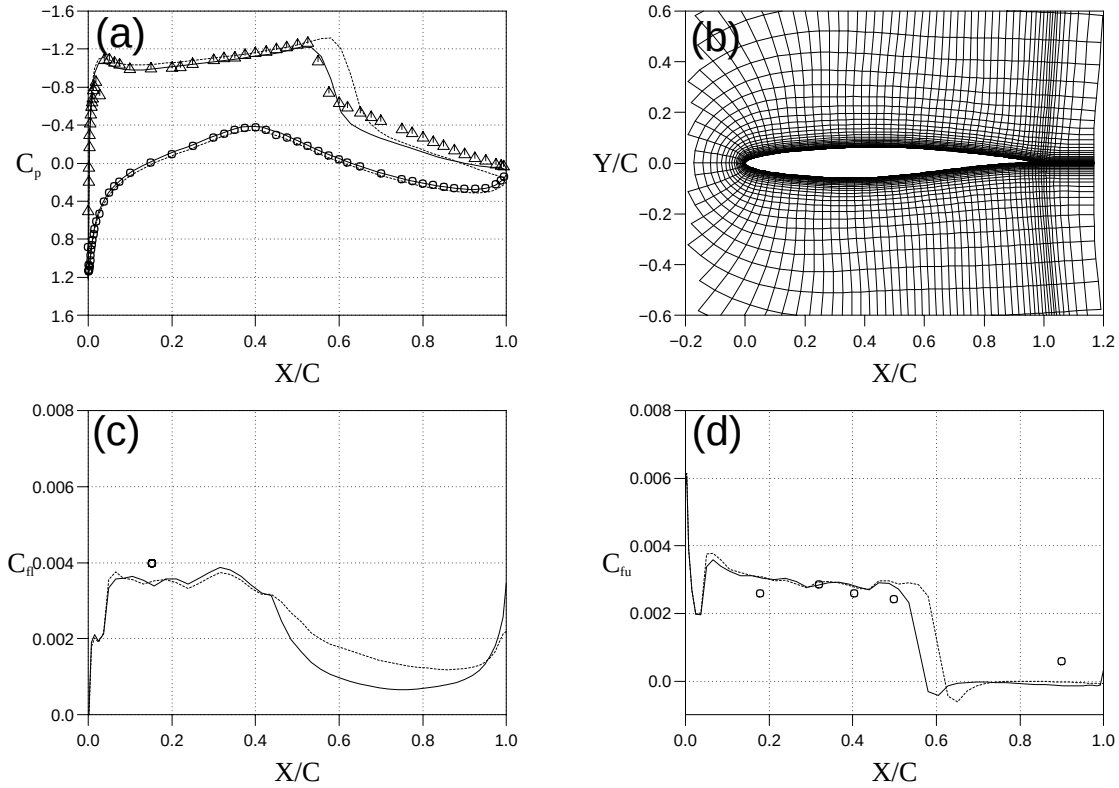

Figure 3: Results for RAE2822 (case 10), o, $\triangle$ experiment; the modified Baldwin-Lomax (filled line); Baldwin-Lomax (dashed line): (a) surface pressure coefficient; (b) close up of the mesh; (c) lower surface skin friction; (d) upper surface skin friction.

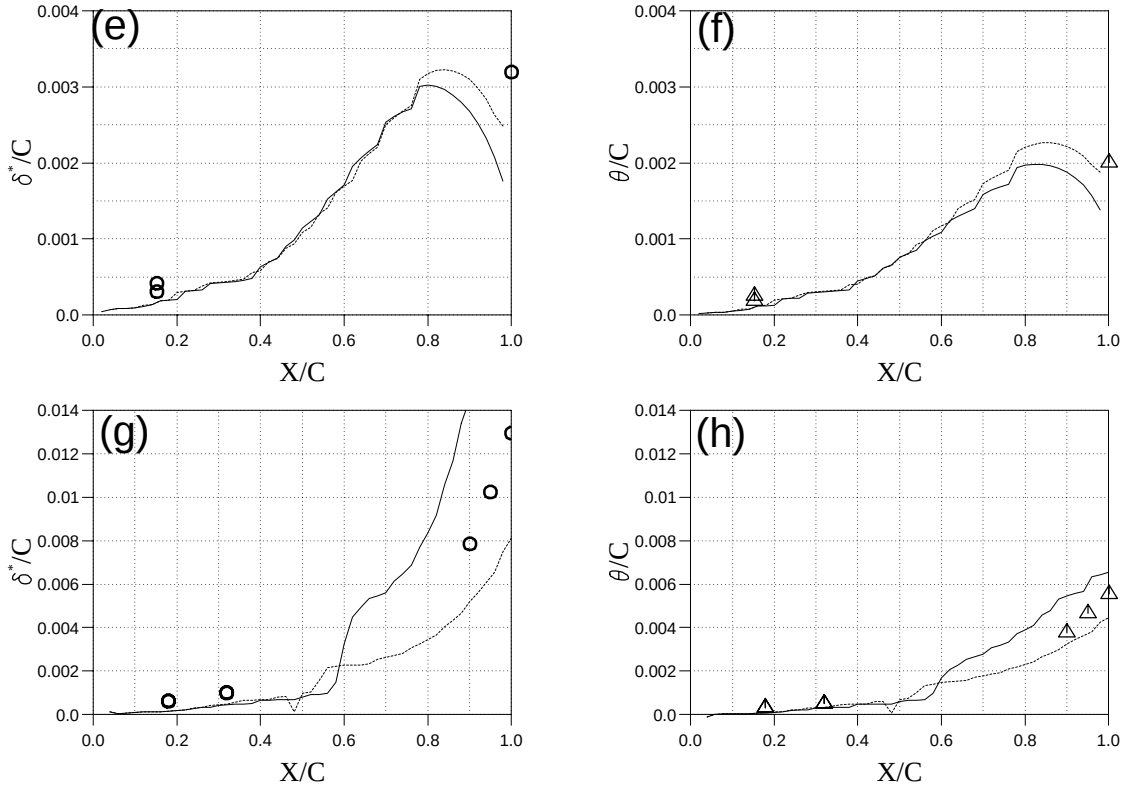

Figure 4: Displacement and momentum thickness for RAE2822 (case 10) at the lower surface (e) and (f), and at the upper surface (g) and (h), respectively; o, $\triangle$ experiment; the modified Baldwin-Lomax (filled line); Baldwin-Lomax (dashed line).

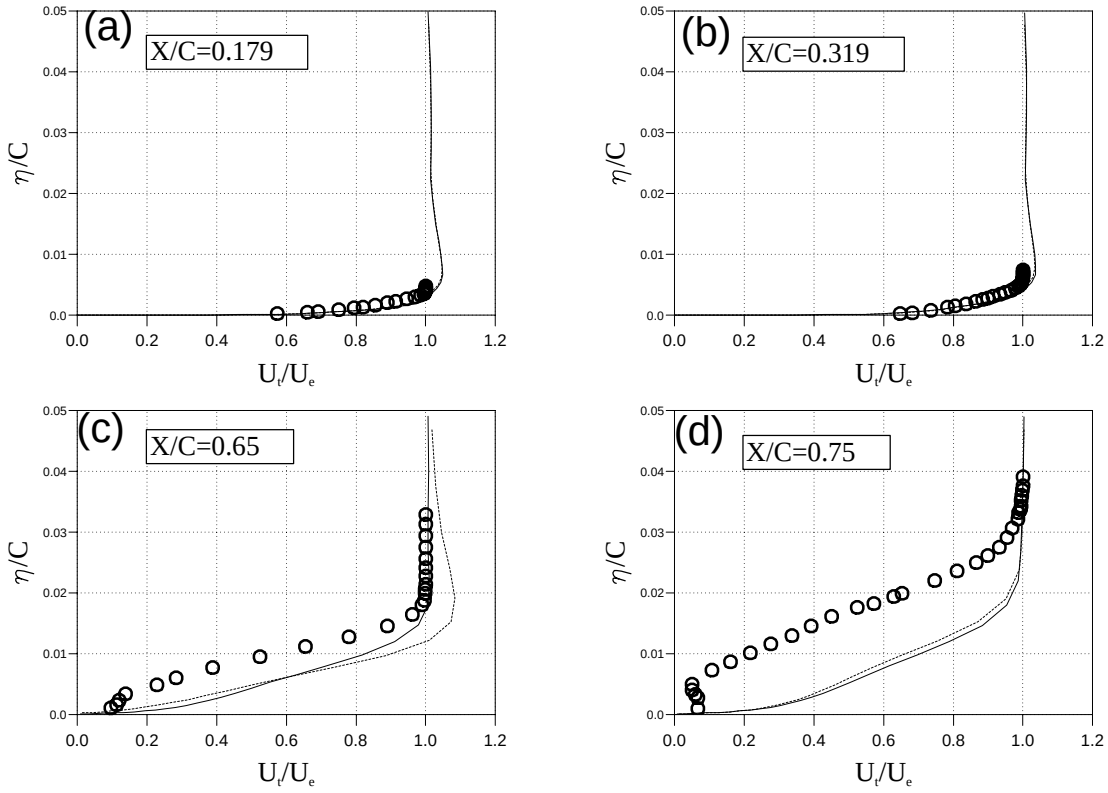

Figure 5: Results for RAE2822 (case 10), *o* experiment; the modified Baldwin-Lomax (filled line); Baldwin-Lomax (dashed line): upper surface mean-velocity profiles at: (a) $X/C = 0.179$, (b) $X/C = 0.319$, (c) $X/C = 0.75$, and (d) $X/C = 0.9$.

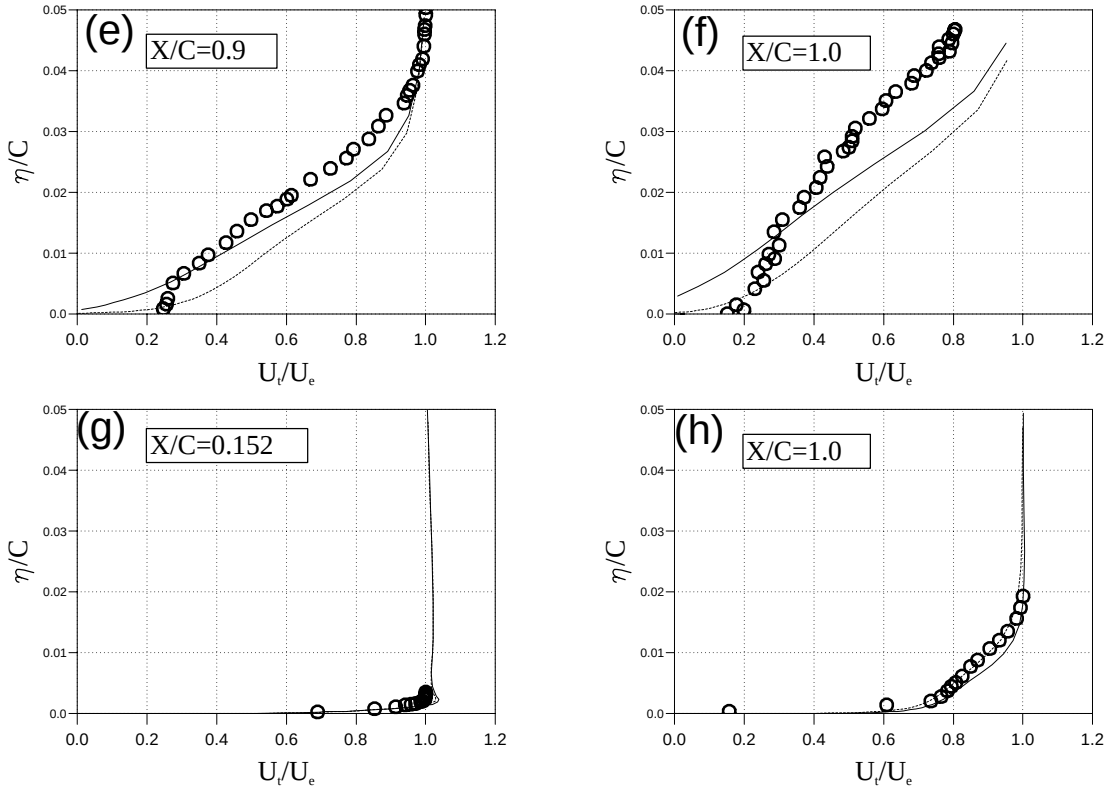

Figure 6: Results for RAE2822 (case 10), *o* experiment; the modified Baldwin-Lomax (filled line); Baldwin-Lomax (dashed line); mean-velocity profiles at the upper surface: (e) $X/C = 0.95$ and (f) $X/C = 1.0$, and at the lower surface: (g) $X/C = 0.152$ and (h) $X/C = 1.0$.

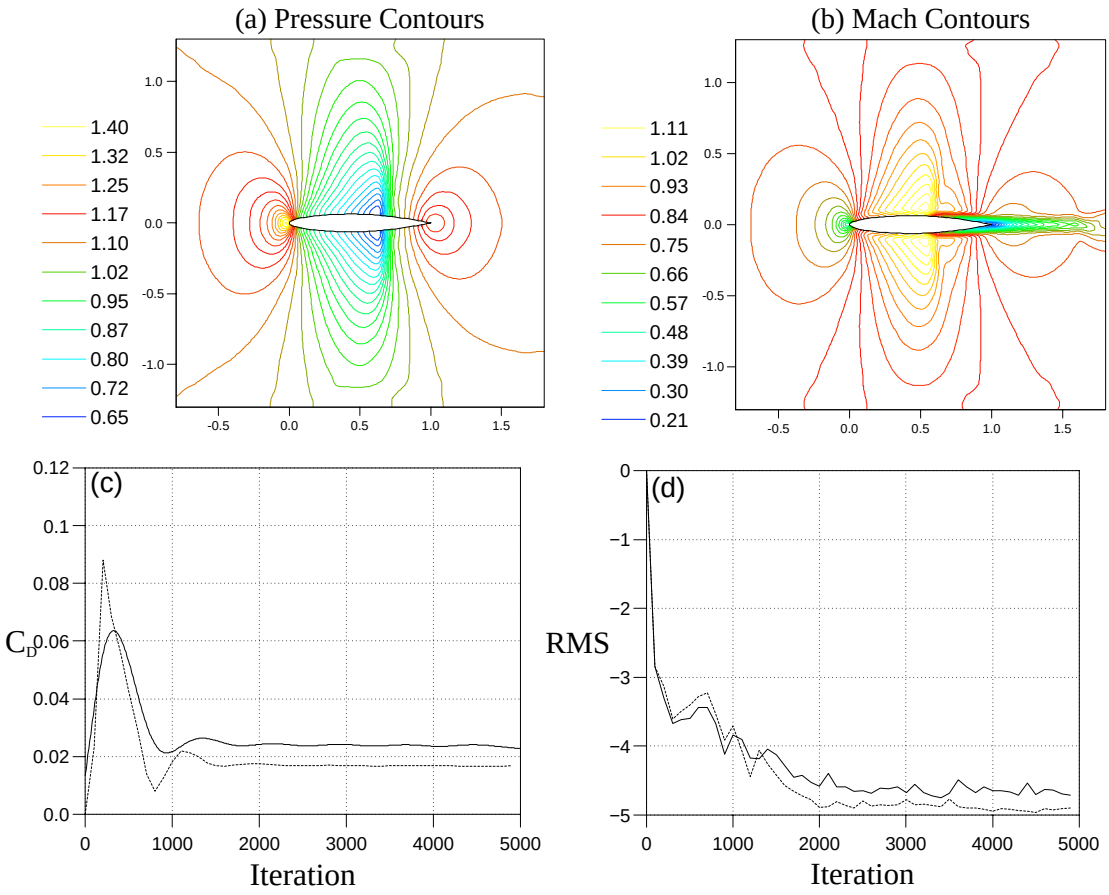

Figure 7: Passive control results obtained for the symmetric RAE2822 aerofoil (case 1: $M = 0.81, \alpha = 0.0^o, R_e = 6.5 \times 10^6$) using Baldwin-Lomax model; (a) pressure contours, (b) Mach contours, (c) drag convergence, and (d) RMS convergence.

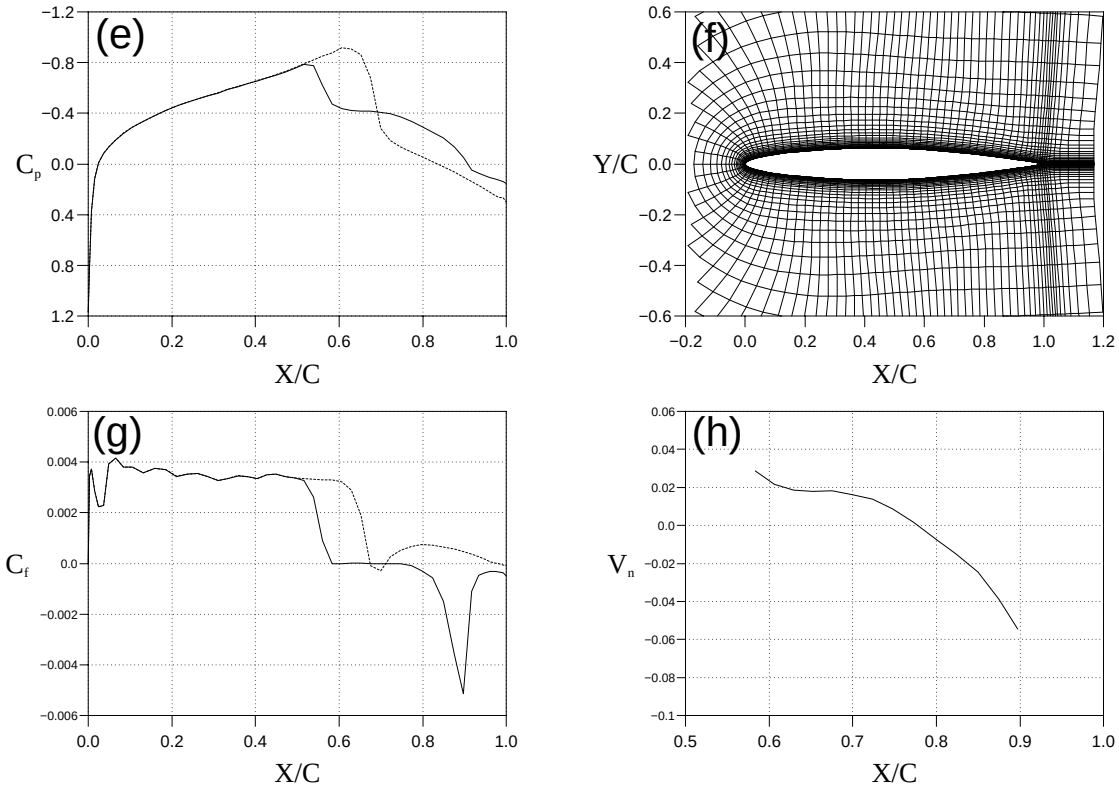

Figure 8: Results for the symmetric RAE2822 aerofoil case 1; porous aerofoil (filled line); solid aerofoil (dashed line); (a) surface pressure coefficient; (b) close up of the mesh; (c) surface skin friction; (d) transpiration velocity distribution.

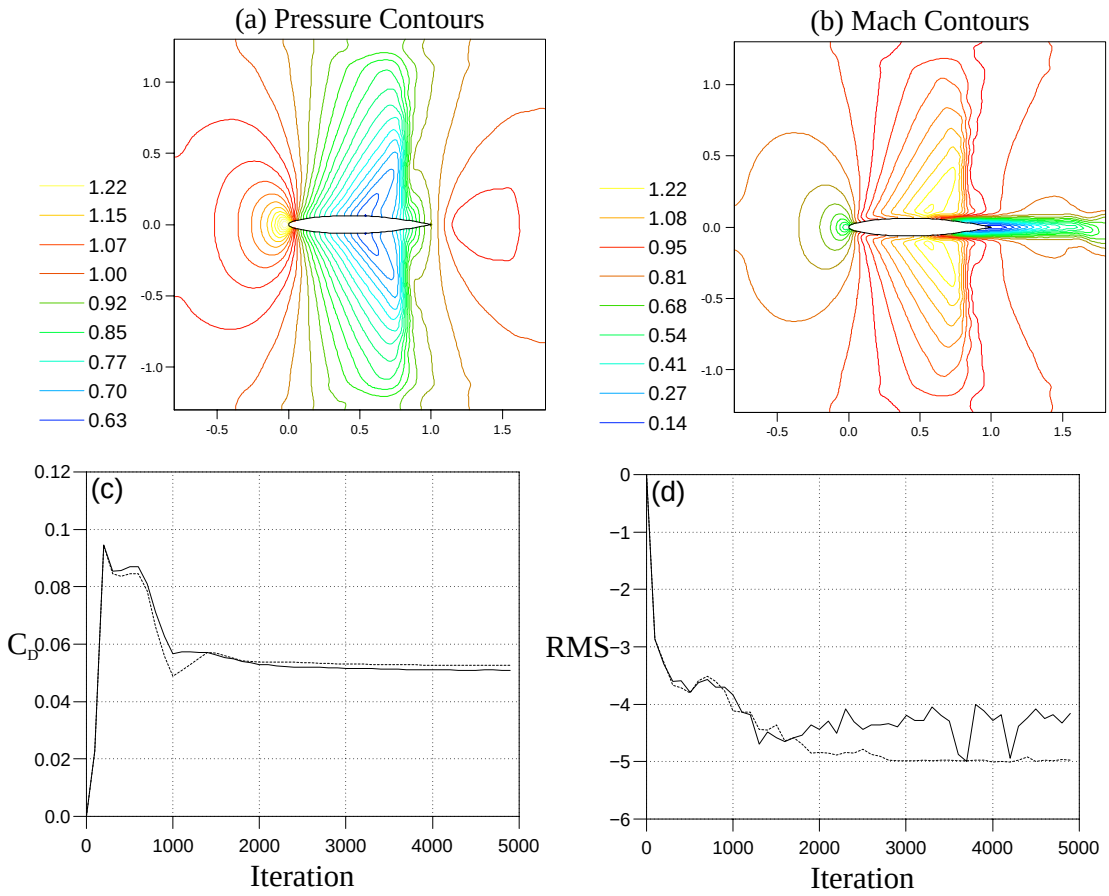

Figure 9: Passive control results obtained for the symmetric RAE2822 aerofoil (case 2: $M = 0.85, \alpha = 0.0^o, R_e = 6.5 \times 10^6$) using Baldwin-Lomax model; (a) pressure contours, (b) Mach contours, (c) drag convergence, and (d) RMS convergence.

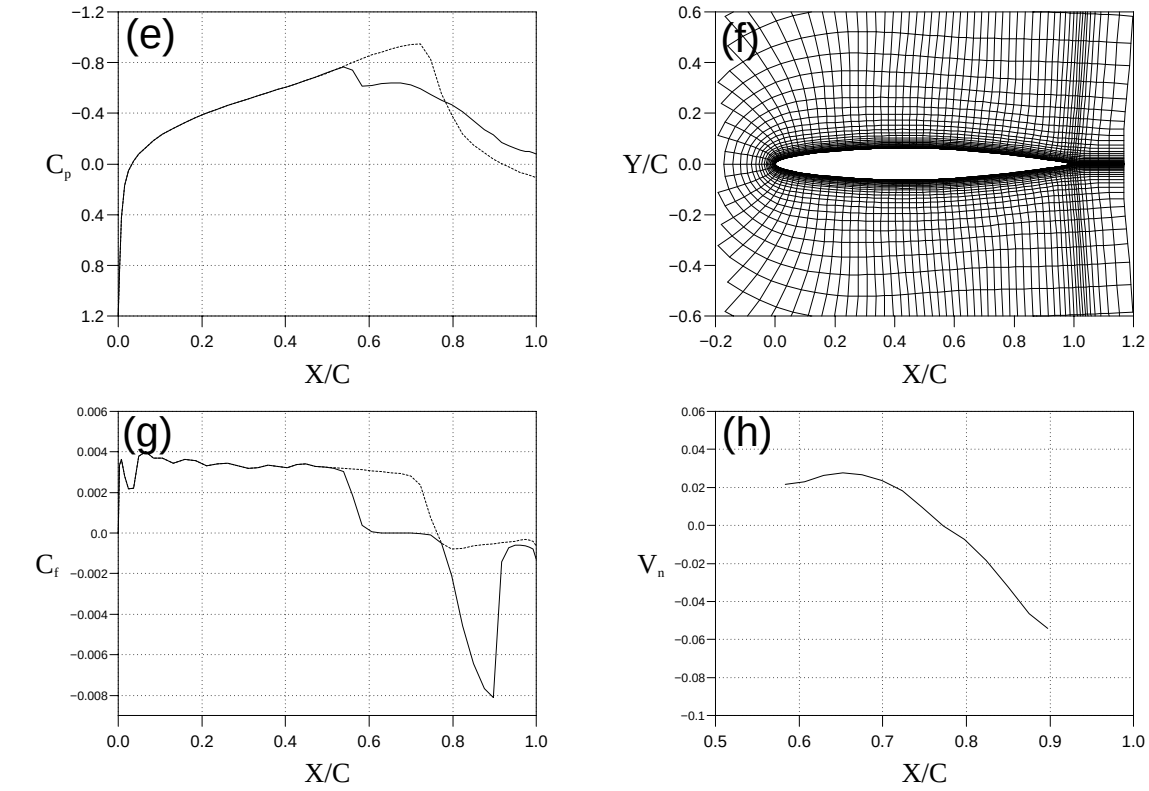

Figure 10: Results for the symmetric RAE2822 aerofoil case 2; porous aerofoil (filled line); solid aerofoil (dashed line); (a) surface pressure coefficient; (b) close up of the mesh; (c) surface skin friction; (d) transpiration velocity distribution.